Structural studies of BSCCO/Ag-tapes by high-energy synchrotron X-ray diffraction

H.F. Poulsen [a,*], T. Frello [b], N.H. Andersen [b], M.D. Bentzon [c], M. von Zimmermann [d]

[a] *Materials Department, Risø National Laboratory, DK-4000 Roskilde, Denmark*
[b] *Condensed Matter Physics and Chemistry Department, Risø National Laboratory, DK-4000 Roskilde, Denmark*
[c] *Nordic Superconductor Technologies, Priorparken 878, DK-2605 Brøndby, Denmark*
[d] *HASYLAB at DESY, Notkestrasse 85, D-22603 Hamburg, Germany*

Abstract

High-energy (100 keV) synchrotron X-ray diffraction has been identified as a powerful tool for characterizing texture and structural phases *within* Ag clad high T_c superconducting tapes of the (Bi,Pb)–Sr–Ca–Cu–O (BSSCO) type during synthesis of $(Bi,Pb)_2Sr_2Ca_2Cu_3O_x$ (Bi-2223) from $(Bi,Pb)_2Sr_2CaCu_2O_x$ (Bi-2212). Using a CCD camera, the texture and concentration of the dominant structural phases can be determined simultaneously within fractions of minutes. As an example, we report on the in situ annealing behavior in air at 835°C of an as-rolled monofilament tape. It is shown that the alignment of the superconducting grains takes place almost exclusively in the Bi-2212 phase. During heating, the texture profile narrows rapidly above 750°C, coincident with the dissolution of $(Ca,Sr)_2PbO_4$. A 98% conversion of Bi-2212 is obtained within 19 h, but furnace cooling leads to the formation of secondary phases such as Bi-2201 and $(Ca,Sr)_2PbO_4$. Room temperature data on similar tapes show that subsequent deformation and annealing results in a higher Bi-2223 phase purity while slightly deteriorating the grain alignment. © 1998 Elsevier Science B.V.

Keywords: BSCCO/Ag tapes; Superconductivity; Synchrotron; Texture; Phase

1. Introduction

A large effort is presently made to process and manufacture high T_c superconducting (HTSC) tapes containing polycrystalline $(Bi,Pb)_2Sr_2Ca_2Cu_3O_x$ (Bi-2223). The tapes are generally fabricated by the powder-in-tube technique, whereby the randomly oriented precursor material consisting mainly of $(Bi,Pb)_2Sr_2CaCu_2O_x$ (Bi-2212) is filled into a Ag tube and converted into textured Bi-2223 within this sheeting. This is done by means of a series of thermomechanical treatments, typically involving various rolling and annealing steps [1]. By varying the annealing temperatures, the deformation rates and the composition of precursor material, the superconducting critical current density, J_c, is optimized. Densities of up to $J_c = 110$ kA/cm^2 have been reported at 77 K and 0 T for short specimens [2],

---

while values of the order 10–40 kA/cm^2 are obtained routinely for meter-long specimens. These values should be compared to reported values of $J_c = 1000$ kA/cm^2 for Bi-2223 thin films (and $J_c > 20$ kA/cm^2 for Bi-2212 thin films [3,4]), measured under similar conditions.

It is generally accepted that J_c may be limited by several factors, including the purity of the superconducting phase, the packing density, and the degrees of inter-grain connectivity and inter-grain alignment. Among these parameters, the texture of the HTSC material has attracted much attention due to the well-known strong electrical anisotropy of the HTSC materials, where the conduction basically is confined to the (a,b)-plane. Data on current transmission across artificially fabricated grain boundaries in Bi-2212 likewise indicate that large angle [001] tilt boundaries are weak links [5]. Moreover, large anisotropies in J_c have been measured in the BSCCO tapes themselves [6,7].

In the past, most laboratories have optimized J_c via an empirical 'black-box' approach. Today, it is accepted that to proceed beyond status quo, it is necessary to investigate the structural development of the tapes during processing in detail. In particular, it is of interest to identify the origin of the texturing and the exact reaction scheme leading to Bi-2223. Finding the answers to these questions has proven difficult, partly due to the complexity of the material, partly due to a lack of suitable characterization tools. Most notably, the Ag sheeting is known to influence the phase diagrams substantially. In situ studies of the kinetics on the tapes themselves are therefore called for. Unfortunately, conventional diffraction tools such as electron microscopy and Cu K α X-rays cannot penetrate silver. Neutrons are also absorbed by silver and the obtainable signal-to-noise ratio with neutron diffraction is discouragingly small [8].

In this paper, we propose to use the novel technique of high-energy synchrotron radiation for structural characterization of the tapes. At 100 keV, X-rays are able to penetrate tapes of typical dimensions in all directions perpendicular to the rolling direction apart from a small angular range of approximately 10°, where the incoming beam is nearly aligned with the transverse direction. Using a 2D detector, we may obtain information about the texture and concentration of the dominant crystalline phases from a single exposure, which typically may be acquired within 30 s.

The paper is organized in the following way. Initially, we present the experimental set-up and explain how the acquired images are reduced to 'conventional' one-dimensional data set. Next, a framework for the texture analysis is established. Then, we present typical results from two sets of tapes—tape A and tape B—manufactured at Nordic Superconducting Technologies (NST). [1] On tape A, room temperature data were acquired after each of the four major processing steps: before and after 1st annealing, and before and after 2nd annealing. On tape B, in situ data were recorded during the 1st annealing. Finally, the general prospect of the technique is discussed.

2. Experimental set-up

An experimental set-up for in situ studies of tapes has been established at the BW5 synchrotron beamline at HASYLAB, Hamburg. The beamline is equipped with a symmetric Wiggler with a critical energy of 26.5 keV, and dedicated to X-ray diffraction experiments with energies above 60 keV [9]. For our purpose, the energy was chosen to be 100 keV, corresponding to penetration depths of $\mu = 650$ μm and $\mu = 600$ μm in Ag and fully dense, pure Bi-2223, respectively.

The geometry of the set-up is illustrated in Fig. 1. The unfocused beam is monochromatized by a single imperfect SrTiO$_3$ crystal with a mosaicity of FWHM $= 40''$, using the (2,0,0) reflection in Laue geometry. A slit is used to define the incoming beam. The gaps are typically set at 1 mm horizontally and 1 mm vertically. With this setting, the incoming flux on the sample is measured to be roughly 1.0×10^{11} photons/s. Powder patterns are recorded on-line on a CCD camera. The camera is a 12-bit tapered XIOS-II version from Photonics Science with an efficiency of 50% at 100 keV, and an effective area of 77×83 mm^2. It is typically operated in a 600×650 pixel
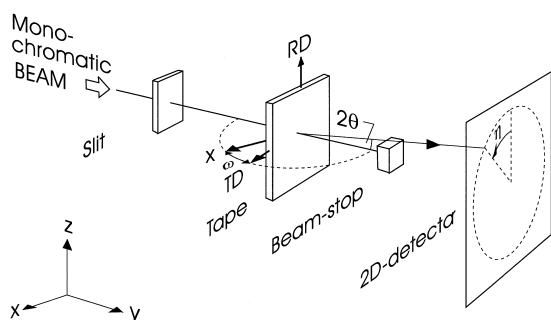
Fig. 1. Schematic of the experimental set-up at beamline BW5, HASYLAB. The definitions of a laboratory coordinate system (x, y, z) and angles 2θ, η, ω are illustrated. RD and TD denote the rolling and transverse directions of the tape, respectively.

mode and at a gain of 2. The read-out-noise and dark current is then of the order 4 counts/pixel and 0.08 counts/pixel/s, respectively, figures that are negligible in comparison to the general background.

A laboratory coordinate system (x, y, z) is defined with the beam along the y-axis and perpendicular to the plane of the detector, cf. Fig. 1. The z-axis is parallel to the vertical axis. The azimuthal angle around the Debye–Scherrer cones is called η. We define η to be 0 along the positive z-axis, and positive in clockwise direction when viewed in the direction of the beam (implying that η will be positive counter-clockwise in the image). Tapes are mounted on a horizontal ω table with the rolling direction (RD) vertically and the normal direction (ND) parallel to the beam for $\omega = 0$. ω is defined as positive counter clockwise when viewed from above.

In general, the camera is mounted as far away from the sample as possible while still retaining slightly more than one quadrant of the relevant diffraction pattern (123.6 cm). The approximate resolution in this geometry is: $\Delta 2\theta = 0.02°$, $\Delta \eta = 1.2°$ and $\Delta \omega = 0.02°$. However, for some reference work on peak shape effects the camera was mounted at the end of the hutch—at a distance of 300 cm—and the gap of the slit in front of the sample was narrowed to 0.5 mm, all in order to increase the 2θ resolution. Estimates of the 2θ resolution was obtained from exposures of pure well-annealed Bi-2223 powders.

For in situ work up to 8, tapes were mounted in parallel in a modified version of the neutron diffraction furnace used in Ref. [10], with 4 of the tapes being fixed at $\omega = 0°$ and 4 at $\omega = 75°$. The incom-

ing and diffracted beam both had to penetrate a 100-μm Ag heat shield, a 2.1 mm quartz tube and 1 mm Al. Two chromel/alumel type thermocouples encapsulated in inconel were used. Detailed information about the furnace will be provided elsewhere.

3. Data analysis

Data analysis is done primarily by means of the software packages FIT2D [11] and CONE [12]. Initially, images are normalized to primary intensity and exposure times, and corrected for spatial distortion in the camera. Next, the centers of the diffraction patterns are found and the traces of the Debye–Scherrer cones in the images are parameterized. The radial offset between the estimated traces and the texture segments in the exposures is found to be less than 1 pixel.

The further data analysis is based on various one-dimensional projections of the images. Three projections are used: 2θ projections, line profiles and texture profiles. 2θ projections contain the radial intensity variation within the image, averaged for each 2θ value over the available η range. They are used for indexing and estimates of phase concentrations. Line profiles contain the intensity variation along a radial line in the image at a given azimuthal angle η. Intensities are averaged over 10 pixels in the direction perpendicular to the radial line. Hence, the data set is equivalent to conventional powder diffractograms obtained by a single detector with an aperture 1 pixel wide and 10 pixels high in front of the detector. Line profiles are used for estimates of the 2θ widths of the individual reflections. Finally, the texture profiles contain the intensity variations with η for fixed 2θ of the powder diffraction segments. For each η position in the texture profile, the scattered intensity in the image is integrated radially within the 2θ range of the reflection. A linear background subtraction is employed.

Once the texture profiles have been found, conventional pole figures in the (ND,TD) plane may be calculated, e.g., using the coordinate transforms given in Ref. [11]. However, our experimental data all indicate that the Bi-2212 and Bi-2223 textures to a good approximation are fiber-symmetric with $(00l)$ aligned along ND. This is in accordance with a series
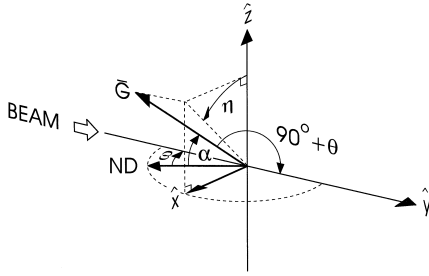
Fig. 2. Definition of the polar coordinate α used for texture analysis of the Bi-2212 and Bi-2223 phases. G is the scattering vector of interest, and ND the normal direction of the tape. Symbols (x,y,z) and θ, η, ω are defined in Fig. 1.

of works performed by other groups [8,13–15]. The interesting distribution is therefore $P(\alpha)$, the probability of finding the scattering vector of interest G, with a spherical distance of α to ND (or to the inverse direction of ND whichever α value is smaller). We will symbolize the width (FWHM) of this profile by $\Delta\alpha$. As illustrated in Fig. 2, the transformation between η and α is given by

$$\cos(\alpha) = |\cos(\theta)\sin(\eta)\sin(\omega) + \sin(\theta)\cos(\omega)|. \tag{1}$$

Due to the rather distinct texturing, the $P(\alpha)$ distributions for different reflections belonging to the same phase will, to a good approximation, have the same peak shape, and therefore also nearly identical $\Delta\alpha$'s.

If the texture is not only fiber-symmetric but also Gaussian, the Taylor expansion of Eq. (1) shows that the FWHM of the η distribution for the $(00l)$ reflections to a very good approximation will be identical to $\Delta\alpha$ for all ω of relevance. However, for other types of distributions such as Lorentzians, the widths of the two distributions may vary by a factor of 2 or more. Generally, extraction of texture widths cannot be based on data related to the $(00l)$ reflections alone, as the central part of the distribution is inaccessible due to absorption.

Within the fibre symmetric approximation, the concentration, c, of the various phases may be found according to

$$c \propto \frac{\sin(\theta)}{\lambda^3 N_0^2\, j_{hkl}|F_{hkl}|^2}\, \frac{1}{VA(\omega,\eta,\theta)} \int I_{\mathrm{norm}}(\alpha)\mathrm{d}\alpha \tag{2}$$

where $|F_{hkl}|^2$ is the structure factor including the atomic form factor, j_{hkl} the multiplicity, N_0 the number of unit cells per unit volume, V the volume of the HTSC core illuminated by the beam, $A(\omega,\eta,\theta)$ the absorption coefficient, and $\int I_{\mathrm{norm}}(\alpha)\mathrm{d}\alpha$ the integrated intensity over the α-distribution (normalized to incoming photon count). For the small scattering angles in the experiments, the variation in the polarization factor may be neglected. However, structure factors are not known for several of the phases of relevance here, either because literature data are scarce (Bi-2223) or because the stoichiometry of the compounds vary, e.g. $(Ca,Sr)_2PbO_4$. For the presentation in this paper, we will, therefore, to some extent, rely on scaling of $\frac{1}{VA}\int I_{\mathrm{norm}}(\alpha)\mathrm{d}\alpha$ to known abundances in the tapes before or after annealing. The exact procedure will be outlined along with the presentation of results.

For calculations of the absorption coefficient, A, we note that the penetration depths of Ag and HTSC are nearly the same at 100 keV. We may therefore approximate the tape geometry by a single slab of thickness t, inclined at an angle $90 - \omega$ to the incoming beam. The following equations apply

$$A(\omega,\eta,\theta) = \exp\left(\frac{d(\omega,\eta,\theta)}{\mu\cos(\omega)}\right), \tag{3}$$

$$d = \frac{tx}{\cos(2\theta)\cos(\omega) - \sin(2\theta)\sin(\omega)\sin(\eta)} + \frac{t(1-x)}{\cos(\omega)},$$

where x is the fractional distance at which the scattering takes place. At $\omega = 75°$, the attenuation is rather large, even at 100 keV. However, due to the small Bragg angles and the rather narrow texture profiles, we may, to a good approximation, substitute Eq. (3) by the $2\theta \to 0$ limit:

$$A(\omega) = \exp\left(-\frac{1}{\mu\cos(\omega)}\right). \tag{4}$$

For the standard data analysis, cf. below-based on the HTSC (115) reflections at $\omega = 75°$, the absolute errors introduced by using Eq. (4) are of the order a few percent. Moreover, when comparing identical reflections of the Bi-2223, Bi-2212 and Bi-2201 $(Bi_2Sr_2CuO_x)$ phases, the relative error will be much smaller. In general, we have therefore neglected

absorption in our texture analysis, while Eq. (4) has been used to normalize integrated intensities when comparing measurements made at different ω's or on different samples.

4. Samples

The two monofilamentary tapes both had a nominal powder composition of $Bi_{1.84}Pb_{0.34}$-$Sr_{1.91}Ca_{2.03}Cu_{3.2}O_{10+x}$. The powder had been calcined at 830°C. The tapes were processed according to the 'standard' scheme, involving four processing steps: (1) drawing and rolling, (2) a first annealing, (3) a second deformation (semi-continuous pressing) and (4) a second annealing. The annealings were done in technical air with subsequent slow cooling obtained by switching the power of the furnace.

Tape A was divided into 4 parts: A1 to A4. These were removed during processing after step 1, 2, 3,

and 4, respectively. Synchrotron measurements were done at room temperature on specimens of each of these. Tape A1 had an average thickness of 260 μm and a width of 2.3 mm, while tape A4 was 190 μm thick and had a critical current density of $J_c = 8$ kA/cm^2 at 77 K. All specimens were 8 cm long. Tape B was used for an in situ study during the first annealing. This tape, which was not heat-treated before the annealing, had an as-rolled thickness of 238 μm and width of 2.44 mm and a final J_c of 7 kA/cm^2. In this case, the specimen used had a length of 4 cm.

5. Results

5.1. Room temperature data

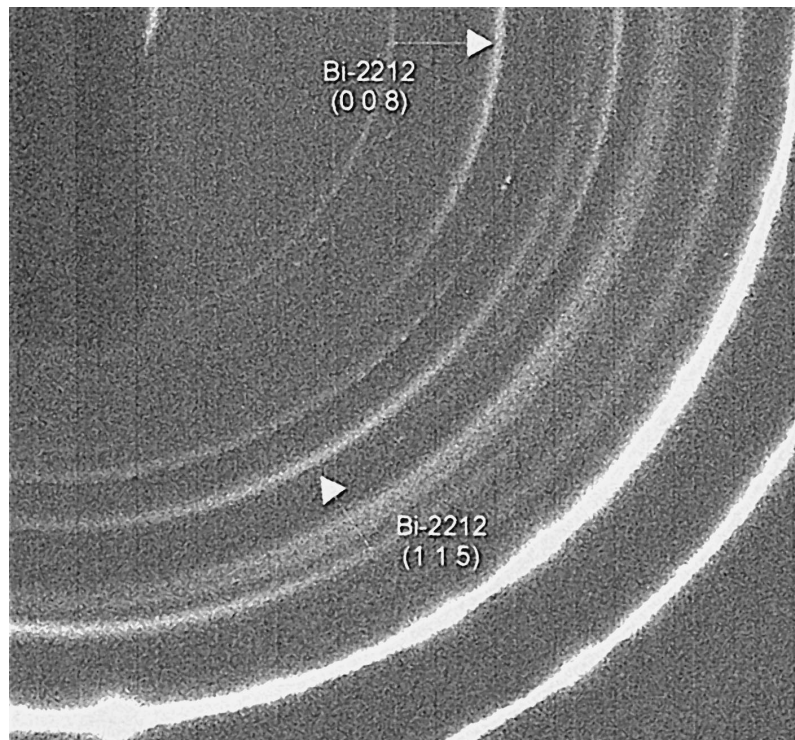Room temperature data—with the tapes mounted outside the furnace—were acquired for tapes A1 to

Fig. 3. Room temperature exposure of the as-rolled tape, Tape A1, at $\omega = 75°$. The image is dominated by the strong lines from the Ag sheet and the Bi-2212 (00l) reflections. To protect the detector, a large beamstop was used, evident as a dark region in the upper left corner. As part of data acquisition, the image is flipped up/down. The left side and the upper rim of the image therefore corresponds to $\eta = 0$ and $\eta = 90$, respectively.
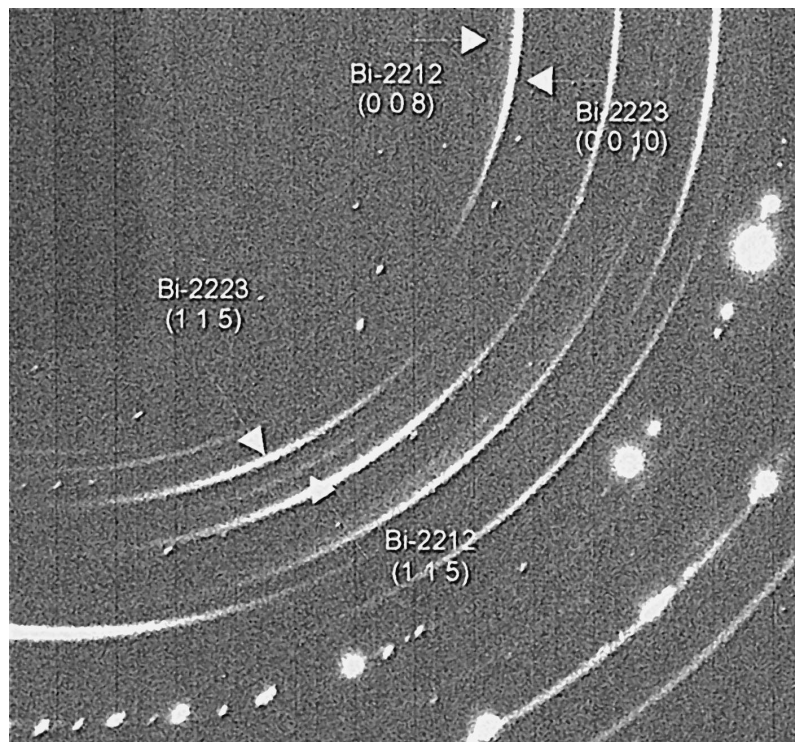
Fig. 4. Room temperature exposure of the fully processed tape, Tape A4, at $\omega = 75°$. The image is dominated by the strong lines from the Bi-2223 (00l) reflections. In comparison to Fig. 3, silver is seen to have recrystallized to form Bragg peaks instead of powder rings. The left side and the upper rim of the image corresponds to $\eta = 0$ and $\eta = 90$, respectively.

A4 using a series of ω settings. To illustrate the data treatment involved, we start by presenting a detailed analysis of the tape A1 and tape A4 data at the two settings $\omega = 0°$ and $\omega = 75°$.

The raw exposures for $\omega = 75°$ are shown in Figs. 3 and 4. Exposure times were 30 s, and the resulting intensities in the main HTSC reflection are of the order 3300 counts/pixel and 700 counts/pixel for process step 1 and 4, respectively. At 2θs below 2.0°, the background is dominated stray scattering from the hutch varying between 60 and 150 counts/pixel. At higher angles, the combined diffuse and Compton scattering from the sample becomes dominant. For the HTSC reflections of main interest here, the two contributions are nearly the same size.

The corresponding 2θ projections are shown for chosen ω settings in Figs. 5 and 6 for tapes A1 and A4, respectively. The indexing procedure involved the structural phases Ag, Bi-2201, Bi-2212, Bi-2223, and $(Ca,Sr)_2PbO_4$. In addition, a line at $d = 2.18$ Å

is present in all data sets. Contributions from higher harmonics $(\lambda/2, \text{etc.})$ are only found for the strongest Ag lines—and easily separated. It should be noted that the information content in the raw images is significantly higher than in the projections. Hence, inspection of the exposure shown in Fig. 4 showed small dots with d-spacings corresponding to the CuO (002)/(111) line, indicating the presence of relatively large and/or perfect CuO particles.

The results of the texture analysis for the Bi-2223 phase in tape A4 are summarized in Fig. 7. The texture profile of the dominant (200) reflection at $\omega = 0°$ is shown as an insert. Evidently the deviation from a uniform profile is of the order 5%, comparable to the degree of fluctuations within the sample. The profile of the chosen (115) standard reflection at $\omega = 75°$ is shown in the main part of the figure—as a function of α, cf. Eq. (1). Also shown is the result of fits to Gaussian, Lorentzian and Lorentzian squared functions. Clearly the Lorentzian squared—

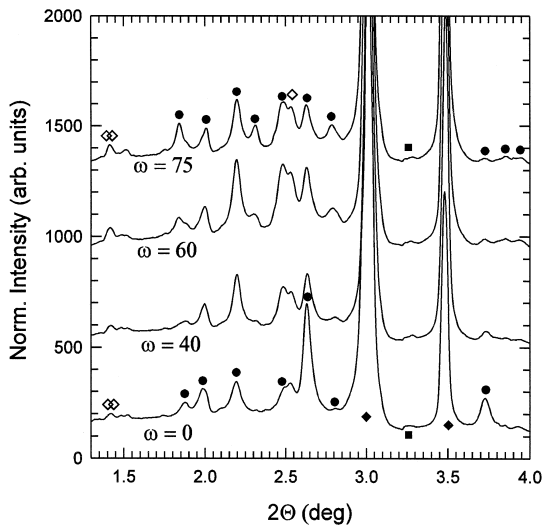Fig. 5. 2θ-projections at various ω settings for Tape A1. The $\omega = 75°$ data are based on an analysis of the image shown in Fig. 3. Intensities are normalized to acquisition time and primary intensity. The 2θ axis is normalized to a literature value for the Ag (111) line. Symbols refer to: (●) Bi-2212, (◆) Ag, and (◇) $(Ca,Sr)_2PbO_4$. A non-identified phase is marked by ■.
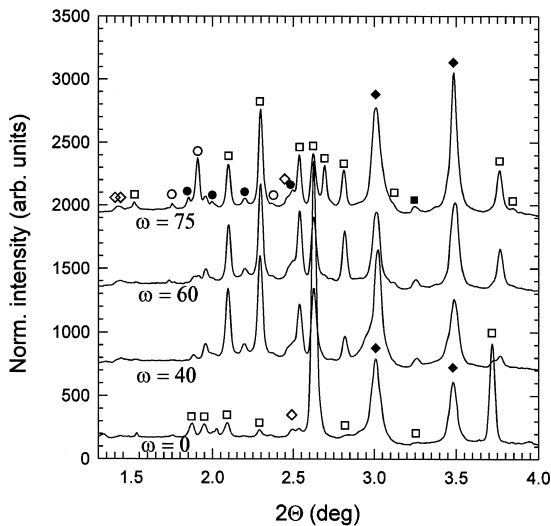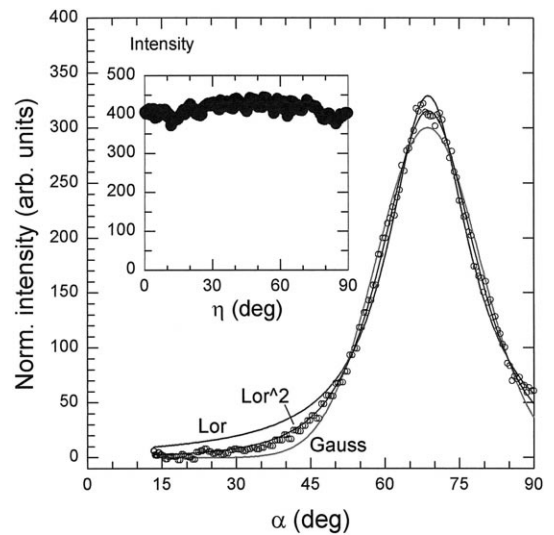

Fig. 7. Texture analysis of Tape A4 (after 2nd annealing). The main part of the figure relates to a Bi-2223 (115) texture profile at $\omega = 75°$. The normalized data (○) are shown as function of α, along with best fits (————) to Gaussian, Lorentzian, and Lorentzian squared functions. The $\omega = 0°$ texture profile of the Bi-2223 (200) reflection is shown in the inset.

Fig. 6. 2θ-projections at various ω settings for Tape A4. The $\omega = 75°$ data are based on an analysis of the image shown in Fig. 4. Intensities are normalized to acquisition time and primary intensity. The 2θ axis is normalized to a literature value for the Ag (111) line. Symbols refer to: (□) Bi-2223, (●) Bi-2212, (○) Bi-2201, (◆) Ag, and (◇) $(Ca,Sr)_2PbO_4$. A non-identified phase is marked by ■.

with a width of $\Delta\alpha = 21.9 \pm 0.2°$—represents the data best. Similar results were obtained for other non-overlapping reflections: (117), (200), (0010), and (0012), with an average width of $\Delta\alpha = 21.4 \pm 1.0°$. Analysis of data obtained at other ω settings complied with these findings, and provided further validation of the assumption of a fibre-symmetric Bi-2223 texture.

The results of an analogue data treatment of the Bi-2212 phase in tape A1 are shown in Fig. 8. Again the deviations from a uniform profile is small at $\omega = 0°$. At $\omega = 75°$, the (115) reflection is, to a minor degree, overlapping with (0010) due to a large 2θ spread, cf. below. After a suitable correction for this effect, the texture data are well described by a Lorentzian square function with best fit for $\Delta\alpha = 59.0 \pm 0.5°$. The corrected data set and the fit are compared in the main part of Fig. 8.

The analysis of the $(Ca,Sr)_2PbO_4$ phase is based on the closely lying (110) and (020) reflections. In the case of Tape A1, the (110) is found to be aligned along ND in an approximate fiber symmetry. The width of the distribution is $\Delta\alpha = 160 \pm 30°$. The data for tape A4 are consistent with a similar type of
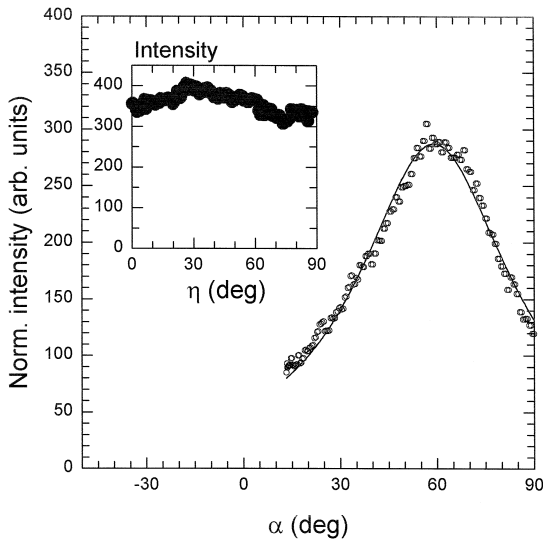
Fig. 8. Texture analysis of Tape A1 (as-rolled). The main part of the figure relates to a Bi-2212 (115) profile at $\omega = 75°$. The normalized data ($\bigcirc$) are shown as function of α, along with a best fit (————) to a Lorentzian squared function. The $\omega = 0°$ texture profile of the Bi-2212 (200) reflection is shown in the inset.
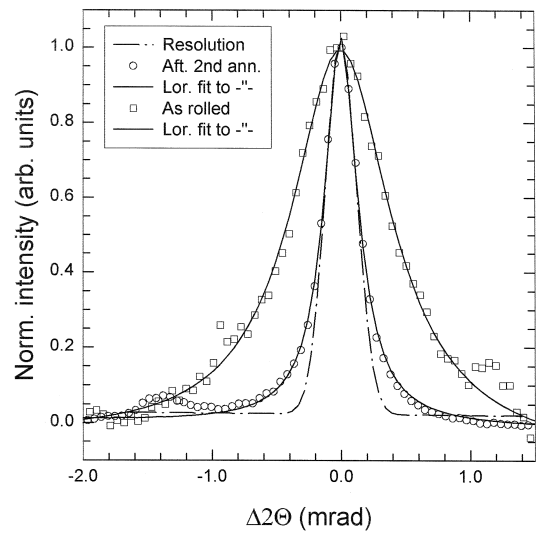

Fig. 9. Peak profiles for the Bi-2212 (0010) reflection of tape A1 (as-rolled) and the Bi-2223 (0014) reflection of tape A4 (after 2nd annealing). The setting is $\omega = 75°$ and $\eta = 90°$, corresponding to horizontal profiles through the upper rim of the images shown in Figs. 3 and 4. For sake of clarity of presentation, the data are normalized to a common maximum of 1. Best fits to Lorentzian peakshapes are shown, with resulting widths (FWHM) of $\Delta 2\theta = 0.93$ mrad and 0.31 mrad, respectively. The resolution function at the d-spacing of the Bi-2223 reflection is indicated as a dashed line.
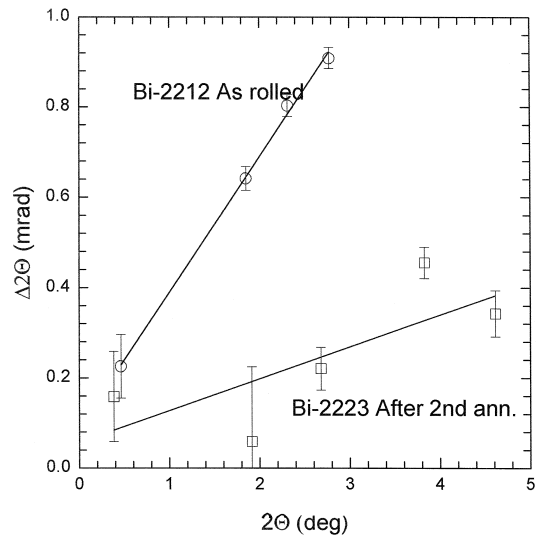
distribution with $\Delta \alpha = 130 \pm 40°$. The texture of the Bi-2201 phase on the other hand is found to be similar to the ones for Bi-2212 and Bi-2223. In this case, the data analysis is based mainly on the (115) reflection.

For the line profile analysis, we start by discussing data related to the set-up with the long sample to CCD distance (300 cm). Line profiles through selected reflections for tapes A1 and A4 are shown in Fig. 9. The data sets are extracted from projections at $\eta = 90°$ through images made at $\omega = 75°$—the same settings as those for the images displayed in Figs. 3 and 4. Both line profiles—as well as the others associated with the reflections of the two phases—are well approximated by Lorentzian peak shapes. The instrumental resolution, on the other hand, as estimated from exposures of a pure Bi-2223 powder, is more Gaussian-like. As expected, the full width at half maximum, $\Delta 2\theta$, for the as-rolled tape is much broader than the width for the fully processed tape, indicating a larger particle size in the A4 tape than in the A1 tape, or relaxation of stresses as a result of the annealing. However, the 2θ variation of $\Delta 2\theta$ of the non-overlapping line pro-

Fig. 10. The full width at half maximum of various (00l) peak profiles as function of 2θ for the standard setting of $\omega = 75°$ and $\eta = 90°$, cf. Fig. 9. Data points are the results of Lorentzian fits throughout. The instrumental broadening has been subtracted. Best linear fits to the points are indicated (————).

Table 1
Structural changes as function of processing steps for tapes A1–A4 (room temperature data)

	Integrated intensities				Concentration (%)			
	2212	2223	2201	CPO	2212	2223	2201	CPO
Reflectance	115	115	115	110 + 020	115	115	115	110 + 020
Tape A1	88 000	–	0	11 800	100	–	0	33
Tape A2	9550	49 000	6600	7000	10.8	81.8	7.4	20
Tape A3	9500	51 000	6900	7100	10.8	81.5	7.7	20
Tape A4	9200	54 000	1400	5300	10.4	88.0	1.6	15

Tape numbers refer to A1: as rolled, A2: after 1st annealing, A3: after 2nd deformation and A4: after 2nd annealing. CPO is short for $(Ca,Sr)_2PbO_4$.
The integrated intensities are determined from texture profiles and involves a correction for absorption, cf. Eq. (4).
Estimates of concentrations are based on the integrated intensities, as explained in the text.

files for the (00l) reflections—shown in Fig. 10—gives evidence that the broadening in both cases are caused predominantly by intergranular stresses with little contribution from particle size effects. This complies well with electron microscopy investigations, which give estimates of 1 μm for the as-rolled grain sizes. From linear fits through the points in Fig. 10, strains of $\varepsilon = -\Delta d/d = 1.7 \times 10^{-2}$ and $\varepsilon = 4 \times 10^{-3}$ is found for the (00l) reflection in (approximately) the ND direction for tape A1 and A4, respectively.

Line profile analysis for the standard set-up with the smaller sample to detector distance has been performed in a similar way. Results were similar but more uncertain due to the poorer resolution.

Table 2
Changes in texture and 2θ widths as function of processing steps for tapes A1–A4 (room temperature data)

	$\Delta\alpha$ (deg)		$\Delta 2\theta$ (mrad)	
	2212	2223	2212	2223
Reflectance	115	115	0010	0014
Tape A1	59.0	–	0.93	–
Tape A2	20.6	20.4		0.30
Tape A3	23.5	25.7		0.33
Tape A4	21.0	21.9		0.31

Tape numbers refer to A1: as rolled, A2: after 1st annealing, A3: after 2nd deformation and A4: after 2nd annealing.
CPO is short for $(Ca,Sr)_2PbO_4$.
$\Delta\alpha$ is the FWHM of the texture profiles, as determined by Lorentzian squared fits to the $P(\alpha)$ distributions—cf. Fig. 11.
The 2θ widths, $\Delta 2\theta$, are the results of Lorentzian squared type fits to the line profile data, without correction for instrumental broadening.

Next, we compare the $\omega = 75°$ results for the 4 processing steps. The determined integrated intensities $\frac{1}{VA}\int I_{norm}(\alpha)d\alpha$ and the resulting concentrations are listed in Table 1. Concentrations are found as follows: the Bi-2212 concentration for step 1, $C_{2212}(1)$, is defined as 100%. Next, $C_{2212}(i)$ is defined with respect to $C_{2212}(1)$, for $i = 2$, 3 and 4. The Bi-2201 and $(Ca,Sr)_2PbO_4$ concentrations are found by means of Eq. (2) by comparison to $C_{2212}(i)$. Finally, the Bi-2223 concentrations—for which reliable structure factors are lacking—are determined by
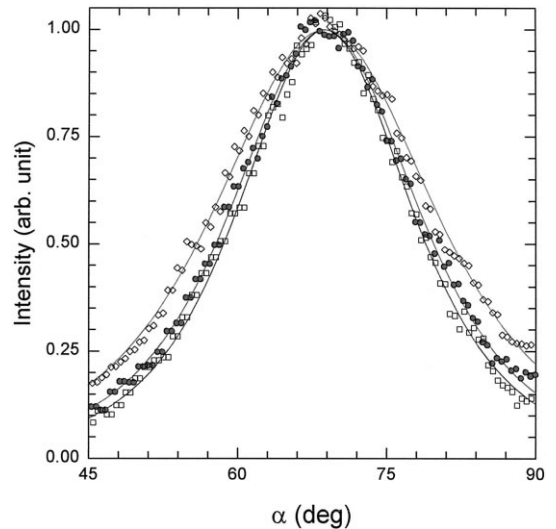

Fig. 11. Texture profiles as function of processing steps for tapes A2 ($\square$), A3 ($\diamondsuit$) and A4 ($\bullet$). Shown are the $P(\alpha)$ distributions for the Bi-2223 (115) reflections, along with best fits to Lorentzian squared functions (————). For sake of clarity of presentation, the 3 graphs are normalized to a peak maximum of 1.

the constraint: $C_{2212}(i) + C_{2223}(i) + C_{2201}(i) = 100\%$. In Table 2, we list the outcome of an analysis of the texture and line profiles. The $P(\alpha)$ distributions for the Bi-2223 (115) reflections are also compared directly in Fig. 11.

From Table 2, the origin of the alignment is clearly seen to be related to the first annealing procedure with $\Delta \alpha$ widths decreasing by approximately a factor of 3. At the same time, the line-width decreases from 0.93 to 0.30 mrad, corresponding to a strain release by a factor 4. The following deformation implies an increase of the widths in both directions, as expected, and the local fluctuations in the system increases as is evident from the more erratic graph for tape A3 in Fig. 11. The second annealing leads to a decrease of widths again—almost but not entirely—to the values obtained after process step 2. From Table 1, the Bi-2223 concentration is seen to increase from step 2 to step 4. Hence, from these data, the second deformation and annealing process appears to be helpful in obtaining a higher Bi-2223 phase purity, while the alignment of the Bi-2223 material actually deteriorates.

Turning next to the secondary phases, the concentration of $(Ca,Sr)_2PbO_4$ drops to 60% of its initial value between steps 1 and 2, and decreases again to a minor amount after the second annealing. The concentration of Bi-2201 on the other hand almost vanished after the second annealing.

In conclusion, the observed effects of the second annealing (increased phase purity, decreased c-axis alignment) are distinct but quite small. We therefore find it likely that the rather large increase in J_c normally obtained by the second annealing is related to other effects such as an improved connectivity between Bi-2223 grains.

5.2. In situ annealing at 835°C

Two specimens of Tape B were inserted in the furnace, one with a setting of $\omega = 0°$ and one at $\omega = 75°$. Annealing took place in an environment of technical air, with an operating temperature of $T_{max} = 835°C$. The 2θ projection of the $\omega = 75°$ data at T_{max} is shown in Fig. 12. The signal is seen to be dominated by the amorphous scattering from the quartz tube. To facilitate an accurate estimate of the background in two dimensions—useful for texture
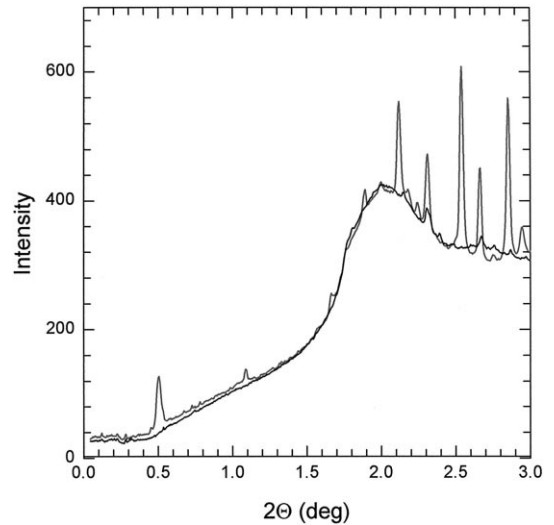

Fig. 12. 2θ projection of an image of Tape B, made at 835°C during in situ annealing at the synchrotron. A background estimate based on the diffraction from a melted tape—useful for texture analysis—is also included. Both data sets are normalized to time and primary intensity and refers to $\omega = 75°$ settings.

evaluations—specimens were heated in situ to the melting point after the annealing procedure of interest here. The 2θ projection of such a 'melted tape background' image is also shown in Fig. 12. The temperature ramp is given in Fig. 13.

The estimated concentration variations of the various phases during the annealing are shown in Fig.
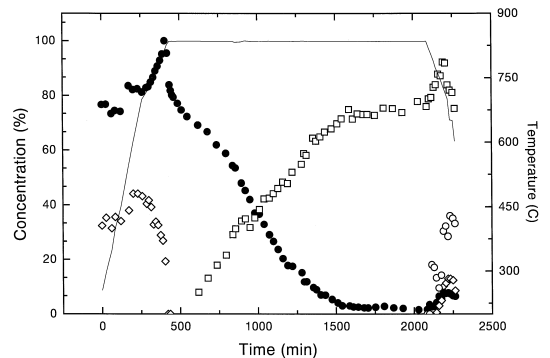

Fig. 13. Relative concentrations of Bi-2212 (●), Bi-2223 (□), Bi-2201 (○) and $(Ca,Sr)_2PbO_4$ (◇) during in situ annealing. The Bi-2201 concentration is multiplied by 10. The analysis is based on the same reflections as those listed in Table 1. The line marks the temperature profile with reference to the temperature scale at the right hand of the figure.
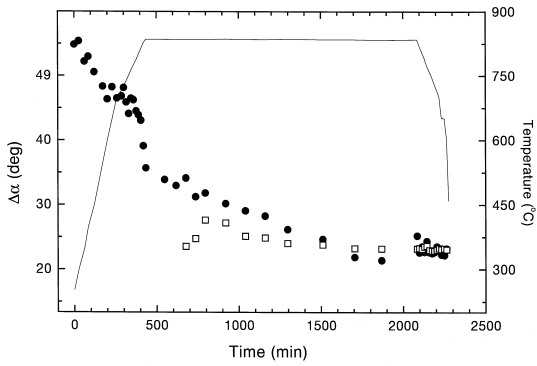
Fig. 14. The width (FWHM) of the texture profiles of the Bi-2212 (●) and Bi-2223 (□) phases. The analysis is based on the (115) reflections, as in Table 2. The line marks the temperature profile with reference to the temperature scale at the right hand of the figure.

13. Corresponding texture results are given for the two main phases in Fig. 14, and in Fig. 15, we present the outcome of a profile analysis from a 2θ projection of the same phases. The data treatment has been similar to what was discussed above in Section 5.1. Finally, the data relating to heating are enlarged and shown as a function of temperature in Fig. 16.

Commenting first on the heating part, we interpret the curves in Fig. 16 as follows: the texture and strain curves are very similar up to 700°C, with
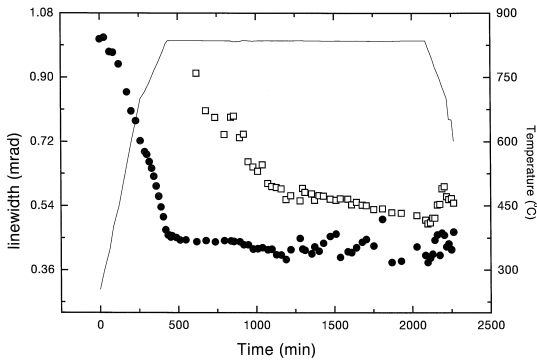
Fig. 15. The 2θ widths (FWHM) of the (115) reflections of Bi-2212 (●) and Bi-2223 (□) as function of elapsed time at the operating temperature during in situ annealing. The data have not been corrected for an instrumental broadening of estimated width 0.35 mrad. The erratic behavior of the Bi-2212 data between 1200 and 2000 min is an artifact of the fitting caused by the low concentration of this phase in this region.
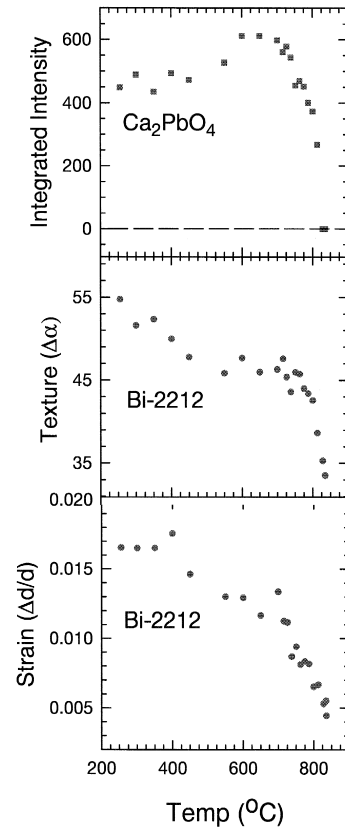
Fig. 16. Summary of structural variations during the heating part of the in situ annealing scheme presented in Figs. 13–15: normalized integrated intensity of $(Ca,Sr)_2PbO_4$ (above), FWHM of Bi-2212 texture profiles (middle) and the residual intergranular strain in the Bi-2212 grains in the approximate ND direction (below). The strain calculations are based on Lorentzian fits to the (0010) line profiles. Texture and intensity data are identical to those presented in Figs. 13 and 14.

approximately constant values in the ranges 0–400°C and 550–700°C. Minor jumps appear at around 450°C. These are attributed to softening of the Bi-2212 material. The increase in the integrated intensity of $(Ca,Sr)_2PbO_4$ at approximately the same temperature is almost certainly an artifact of the analysis, perhaps related to peak shape changes. Between 700°C and 835°C, the three curves all drop dramatically from one plateau to another (cf. also Figs. 14 and 15). $(Ca,Sr)_2PbO_4$ is completely dissolved at 820 ± 5°C. The estimated half-value points for the changes are 770°C, 810°C and 820°C, for strain, $(Ca,Sr)_2PbO_4$ and texture evolution, respectively.

Moreover, we find that with a time lack of 15 min, the texture and $(Ca,Sr)_2PbO_4$ curves are very similar. These findings are all consistent with grain growth of Bi-2212 [16], facilitated by the formation of a partial melt formed by the dissolution of $(Ca,Sr)_2PbO_4$ and possibly other secondary phases.

Relating next to Fig. 13, the concentrations C_{2212} and C_{2223} have been determined by the constraints

$$C_{2212} = 1 \quad \text{when reaching } T_{max},$$

$$C_{2212} + C_{2223} = 1 \quad \text{at } T = 730°C \text{ during cooling.} \tag{5}$$

Results for secondary phases are based on scaling to the Bi-2212 phase by means of Eq. (2). Several features of this plot deserves a comment. First, we note that there is a distinct increase in the integrated intensity of the Bi-2212 phase above 700°C during heating. This effect is likely to be caused by either an additional calcination (the precursor Bi-2212 powder may have decomposed during cooling) or by changes in the Bi-2212 structure factors caused by incorporation of Pb. Next, we note that the transformation of Bi-2212 comes to a stop after 19 h at T_{max} with a final degree of transformation rate equal to 97.5%. The Bi-2223 curve also levels out after 19 h. However, during cooling, a substantial increase in both phases is found, indicating that not all of the Bi-2212 phase material was transformed into Bi-2223. Finally, we note that the secondary phases $(Ca,Sr)_2PbO_4$ and Bi-2201 appears during cooling, at 780°C and 810°C, respectively.

By comparison of Figs. 13 and 14, it is immediately clear that most of the texture development has taken place before the Bi-2212 to Bi-2223 phase conversion. Next, we observe from Fig. 14 that the $\Delta\alpha$ widths of the two phases are identical within experimental uncertainty within the second half of the time evolution. Such a behavior is consistent with the phase transformation taking place via an intercalation process into the existing Bi-2212 grains [17]. The difference between curves at the beginning of the transformation process may indicate that intercalation is faster in well-aligned Bi-2212 grains, e.g., positioned near the HTSC/Ag interface. The final width of the Bi-2223 distribution is $\Delta\alpha = 23 \pm 1°$.

The line profiles of the Bi-2212 (115) and Bi-2223 (115) peaks are shown in Fig. 15. While the Bi-2212

peak remains dominated by the instrumental resolution when T_{max} is reached, there is a distinct broadening of the Bi-2223 peaks. Initially, these are well described by Gaussians, as expected. By a simple analysis of the 2θ variation of $\Delta 2\theta$ along the lines summarized in Fig. 10, we find the Bi-2223 thickness along the c-axis to approach 600 Å asymptotically. This number compares well with results from electron microscopy indicating a layer-by-layer growth of Bi-2223 along the c-axis with spacings in this range.

Cooling was done at a rate of approximately 60°C/h. As evident from Fig. 13, the Bi-2212 content increased significantly along with the development of the secondary phases: $(Ca,Sr)_2PbO_4$ and Bi-2201. The $(Ca,Sr)_2PbO_4$ phase was weakly textured—if at all—while the Bi-2201 had the same texture as Bi-2212/Bi-2223. Note also that the Bi-2223 concentration decreases by 20% during the second half of the cooling procedure (data below 600°C has not been included, as tapes started to move out of the beam due to the difference in thermal expansion between the tape and the sample holder). These results clearly indicate that room temperature data, such as those presented above in Section 5.1, cannot stand alone.

6. Discussion

This experiment is, to our knowledge, the first exploitation of hard X-rays ($E > 60$ keV) for powder diffraction in general. We believe the method developed here to be of general use for in situ studies of polycrystalline materials in complicated sample environments, e.g., during processing. The major drawback is the rather poor longitudinal resolution in Q-space, which is related to the small Bragg angles. However, for many applied problems—including the present one—this may be acceptable.

Based on the present analysis, we estimate that the integrated intensities and the widths $\Delta\alpha$ and $\Delta 2\theta$ of the Bi-2212 and Bi-2223 phases are determined within 5% on an absolute scale. That number is, in our opinion, adequate for a bulk technique. To progress further, it will be useful to be able to probe also the local variations, e.g., as function of distance to the Ag/HTSC interface in monofilamentary tapes

or as function of filament in multifilament tapes. In this context, it is interesting that several options recently have been given for focusing the hard X-rays to one or two-dimensional spots [18–20]. In particular, a 1.2-μm line focus with a resolution of $\Delta d/d \approx 2 \times 10^{-4}$ has been demonstrated at 90 keV [18].

We should point out that in order to perform transmission studies of the tapes, it is not necessary to go to 100 keV X-rays. Provided the available ω range is restricted to below 30°, it is sufficient to use energies slightly below the Ag K edge. Thurston et al. [21,22] has realized this and performed an extensive set of measurements at 24.5 keV at the NSLS synchrotron. Their work, which has been performed over roughly the same time interval (cf. our preliminary report [23]) but independently from ours, is based on the use of a scintillation counter in a two-axis set-up.

Comparing the two approaches, our method has some distinct advantages. First, the enlarged ω range allows us to distinguish between the texture of Bi-2212 and Bi-2223 (at $\omega \leq 30°$ only the overlapping $(h,k,0)$ reflections are available) and to characterize anisotropies in the (a,c)-plane, e.g., grain growth. Second, the diminished absorption corrections make it possible to perform structure refinements including Rietveld analysis. Third, the use of a 2D detector allows for a more extensive data collection, for treating large quantities of samples in parallel—relevant for optimization of processing parameters—and improves conditions for kinetic studies. On the other hand, local investigations of the Ag/HTSC interface can easily be performed with the 24.5 keV set-up [21,22].

At present, we have investigated some 60 tapes in situ by means of the dedicated set-up at HASYLAB. The data presented here are typical of our findings. Detailed parameter studies of the variation of structural properties with temperature, oxygen partial pressures, etc., are in progress.

7. Conclusion

A dedicated set-up for in-situ X-ray diffraction studies of HTSC tapes has been established on a high-energy synchrotron beamline. Adequate quantitative information about phase concentrations, texture, strain and grain size properties of the dominant crystalline phases may be extracted. In addition, complementary microscopy work can be done on the same specimens afterwards to obtain information on local behavior and amorphous/nanocrystalline phases. The methods developed may be of general interest for in situ studies of polycrystalline materials in complicated sample environments.

Acknowledgements

References

[1] K. Heine, J. Tenbrink, M. Thoner, Appl. Phys. Lett. 55 (1989) 2441.

[2] M. Lelovic, P. Krishnaraj, N.G. Eror, U. Balachandran, Physica C 242 (1995) 246.

[3] D. Buhl, T. Lang, J.C. Gauckler, Supercond. Sci. Technol. 10 (1) (1997) 32.

[4] J. Arnold, A. Pfuch, J. Borch, K. Sach, P. Seidel, Physica C 213 (1993) 71.

[5] M. Kawasaki, E. Sarnelli, P. Chaudhari, A. Gupta, A. Kussmaul, J. Lacey, W. Lee, Appl. Phys. Lett. 62 (1993) 417.

[6] K. Sato et al., IEEE Trans. Magn. 27 (1991) 1231–1234.

[7] A. Oota, M. Funakura, J. Iwaya, H. Matsui, K. Mitsuyama, Physica C 212 (1993) 22.

[8] H.-R. Wenk, D. Chateigner, M. Pernet, J. Bingert, E. Hellström, B. Ouladdiaf, Physica C 272 (1996) 1.

[9] R. Bouchard, D. Huppfeld, T. Lippmann, J. Neuefeind, H.-B. Neumann, H.F. Poulsen, U. Rütt, T. Schmidt, J.R. Schneider, J. Süssenbach, M.V. Zimmermann, J. Synchrotron Rad., submitted.

[10] J. Als-Nielsen, N.H. Andersen, C. Broholm, K.N. Clausen, B. Lebech, M. Nielsen, H.F. Poulsen, IEEE Trans. Magnetics 25 (1989) 2254.

[11] A.P. Hammersley, S.O. Svensson, M. Hanfland, A.N. Fitch, D. Häusermann, High Pressure Res. 14 (1996) 235.

[12] R.F. Jensen, J. Schou, J.M. Carstensen, H.F. Poulsen, S. Garbe, J. Appl. Cryst, submitted.

[13] A.D. Rollett et al., Textures and Microstructures 14–18 (1991) 355.

[14] W. Lo, R. Stevens, R. Doyle, A.M. Campbell, W.Y. Liang, J. Mater. Res. 10 (1995) 2433.

[15] J.M. Yoo, K. Mukherjee, J. Mater. Sci. 29 (1994) 4306.

[16] N. Merchant, J.-S. Luo, V.A. Maroni, G.N. Riley Jr., W.L. Carter, Appl. Phys. Lett. 65 (1994) 1039.

[17] W. Bian, Y. Zhu, Y.-L. Wang, M. Suenaga, Physica C 248 (1995) 119.

[18] H.F. Poulsen, S. Garbe, T. Lorentzen, D. Juul Jensen, F.W. Poulsen, N.H. Andersen, T. Frello, R. Feidenhans'l, H. Graafsma, J. Synchrotron Rad. 4 (1997) 147.

[19] P. Suortti, C. Schulze, J. Synchrotron Rad. 2 (1995) 6.

[20] U. Lienert, S. Garbe, O. Hignette, V. Honkimäki, A. Horsewell, M. Lingham, H.F. Poulsen, C. Schulze, N.B. Thomsen, E. Ziegler, J. Synchrotron Rad., submitted.

[21] T.R. Thurston, U. Wildgruber, N. Jisrawi, P. Haldar, M. Suenaga, Y.L. Wang, J. Appl. Phys. 79 (1996) 3122.

[22] T.R. Thurston, P. Haldar, Y.L. Wang, M. Suenaga, N. Jisrawi, U. Wildgruber, J. Mater. Res. 12 (4) (1997) 891.

[23] H.F. Poulsen, T. Frello, N.H. Andersen, M.D. Bentzon, R.F. Jensen, J. Süssenbach, D. Novikov, HASYLAB Jahresbericht, 1995.